Numerical and experimental study of melt instabilities during spot laser welding of aluminium

B.F. Chetan[1,2]*, M. Courtois[2], S. Cadiou[2], M. Carin[2], V. Nain[1], F. Machi[1]

1. IREPA LASER, Parc d'Innovation, 67400 Illkirch, France.
2. Univ. Bretagne Sud, UMR CNRS 6027, IRDL, F-56100 Lorient, France.
* Corresponding author. E-mail address: fchetan@irepa-laser.com

Abstract

Materials such as aluminium with high thermal and electrical conductivities are of industrial interest, particularly for the automotive industry in the current context of increasing production of electric vehicles. The reflective properties of this material make it difficult to process by laser welding. In addition, advances in laser technology offer a broad range of operating parameters and pose a challenge in identifying optimal process parameters. These reasons explain the need for numerical simulation to predict melt pool instabilities and the potential resulting defects such as porosity. A 2D axisymmetric thermohydrodynamic model under static pulse is developed. The laser-matter interaction is described using an equivalent approach to represent the multiple reflections effect of the laser. Vaporisation is simulated by adding a source term to the continuity equation. Tracking of the free interface is treated with a modified Level Set method that preserves mass loss. Experiments validate the results.

Keywords: Laser welding; keyhole; Level set; hydrodynamic; moving interface; numerical modelling

1.   Introduction

Thanks to their lightweight, aluminium alloys are increasingly widespread in automotive, aerospace, and railway transportation, etc. Laser welding is one of the conventional methods for assembling aluminium alloys due to numerous advantages such as speed, flexibility, and narrow welds.

This process consists of melting materials (locally) with a high-intensity heat source, the laser. The melted zone cools down, resolidifies, and forms the weld seam. Initially, the laser beam interacts with a solid material that heats up progressively by conduction until the melting temperature. One gets the melt pool that continues to heat up to boiling temperature, and, at this stage, the matter starts to evaporate. Consequently, the action-reaction principle creates a reactive force, so-called recoil pressure. It is applied at the surface of the melt pool and bends it gradually to create the keyhole (KH), which is filled with escaping metallic vapour.

In spot laser welding, the energy deposition is so localized that it results in the formation of deep KH and a small heat affected zone. This industrial interest in the process is limited by melt pool instabilities, which are generally characteristic of deep KHs and may lead to undesirable defects such as porosities or spatters. These issues are particularly significant in the case of aluminium.

For a better understanding of the complex mechanisms involved in laser welding, numerous studies have focused on the thermohydrodynamic behaviour of the melt pool.

Matsunawa [1] is one of the authors who provided the first notable works on the subject. He studied the dynamics of KH and molten pool using a purely experimental approach, paying particular attention to porosity formation. In addition to understanding the phenomena, predictive tools are needed to improve the welding process. For this reason, most recent studies have developed numerical or coupled numerical-experimental approaches. Thus, Courtois [2] has developed a complete numerical model describing all phase changes during laser welding: from the solid base to the liquid phase, then to metal vapour. Heat transfer and fluid dynamics were solved, and the free interface liquid-vapour was tracked with the Level set (LS) method to predict porosities. The main originality of his work concerns the modelling of keyhole multiple reflections (MR) by considering the laser beam under its waveform and consequently solving Maxwell's equations. Experimental measurements have demonstrated the model's consistency. However, electromagnetic problems require fine meshing and become computationally expensive when solved in 3D. To address this issue,

authors such as Daligault [3] and Mayi [4] used a geometrical optics approach, the Ray-tracing method, to calculate the MR inside the keyhole with COMSOL Multiphysics®. They also modelled the metal vaporisation, which is known to have considerable influence on both the temperature field in the melt pool and its shape. However, these authors had to make sophisticated developments with JAVA to integrate the Ray-tracing method in COMSOL software, which is hardly conceivable in the current work, due to the industrial context.

So, we propose here a simpler model dedicated to the multi-physical simulation of spot laser welding at a mesoscopic scale. The 2D axisymmetric model developed under COMSOL Multiphysics® solves heat transfer, fluid dynamics problems and vapour-liquid interface tracking, the latter with the LS method. A solution is proposed to improve the well-known excessive mass loss inherent to the LS method. Metal vaporisation is modelled to dig the capillary with suitable recoil pressure and reproduce a coherent vapour flow. Without addressing the phenomenon of MR at this stage of the study, its overall effect of increasing absorptivity is taken into account thanks to an easy-to-implement analytical formula.

2. Numerical modelling

2.1. Governing equations

The LS transport equation is:

$$\frac{\partial \phi}{\partial t} + \vec{u}.\vec{\nabla}\phi = \dot{m}\left(\frac{1-\phi}{\rho_v} + \frac{\phi}{\rho_l}\right)\delta(\phi)$$
$$+ \gamma_{ls}\,\vec{\nabla}.\left(\epsilon_{ls}\,\vec{\nabla}\phi\right.$$
$$\left. - \phi(1-\phi)\frac{\vec{\nabla}\phi}{|\vec{\nabla}(\phi)|}\right) \quad (1)$$

ϕ is the LS variable that takes 0 in pure gas and 1 in pure dense metal. Any intermediate value represents a mixture of the two phases. The metal-liquid interface is localised at the isovalue 0.5.

The heat transfer is governed by transient heat law:

$$\rho c_{p,eq}\left[\frac{\partial T}{\partial t} + \vec{\nabla} \cdot (\vec{u}\,T)\right]$$
$$= \vec{\nabla}.\left(k\,\vec{\nabla}T\right)$$
$$+ \left(q_{laser} - q_{evap}\right).\delta_1(\phi) \quad (2)$$

Absorbed laser energy q_{laser} and energy loss by evaporation q_{evap} are volume source terms introduced by a semi-Dirac function, δ_1 defined

from the classical Dirac function δ, which restricts the energy deposition to the dense matter [5] :

$$\delta_1(\phi) = \begin{cases} 0, & if\ \phi \leq 0.5\ (gas) \\ 2\delta(\phi), & if\ \phi > 0.5\ (metal) \end{cases} \quad (3)$$

$$q_{laser} = \alpha_G \cos(\theta)\frac{P_{laser}}{\pi w(z)^2}f(r)g(t) \quad (4)$$

$g(t)$ is the temporal profile of the laser pulse and $\theta[rad]$ the incidence angle. The spatial profile of the laser energy is Gaussian type (Eq. 5), and the beam divergence is considered (Eq. 6).

$$f(r) = N_{laser}exp\left(-N_{laser}\frac{r^2}{w(z)^2}\right) \quad (5)$$

$$w(z) = r_{laser}\sqrt{1 + \left(\frac{z}{z_R}\right)^2} \quad (6)$$

Absorptivity α_G is from Gouffé's model [6]. This formulation of energy deposition means that the absorptivity remains at a constant value of A_0 as long as the melt pool is not deflected. But from an aspect ratio of 0.5, the absorptivity increases and tends towards 1 for $e/d > 10$.

$$\alpha_G = \begin{cases} A_0, & if\ e/d \leq 0.5 \\ \dfrac{A_0\left[1 + (1-A_0)\left(\frac{s}{S} - \frac{s}{S_0}\right)\right]}{A_0\left(1 - \frac{s}{S}\right) + \frac{s}{S}}, & if\ e/d > 0.5 \end{cases} \quad (7)$$

e/d: aspect ratio (KH depth/KH opening); s[m²]: opening section of the KH; S[m²]: the total surface of a paraboloid of dimensions e and d, including the opening section; S₀[m²]: the surface of the sphere of depth d.

$$q_{evap} = \dot{m}L_v \quad (8)$$

$$\dot{m} = (1 - \beta_r)\sqrt{\frac{M}{2\pi RT}}P_{sat}(T) \quad (9)$$

$$P_{sat}(T) = P_{atm}exp\left[\frac{ML_v}{RT_v}\left(1 - \frac{T_v}{T}\right)\right] \quad (10)$$

$\dot{m}[kg/m^2/s]$ mass vaporisation flux; $P_{sat}[Pa]$: saturated vapour pression; R[J/mol/K]: ideal gas constant; M [kg/mol]: molar mass of aluminium.

Mass (Eq. 11) and momentum (Eq. 13) equations are solved assuming incompressible and Newtonian fluids that undergo laminar flow.

$$\vec{\nabla} \cdot (\vec{u}) = \dot{m}\left(\frac{1}{\rho_v} - \frac{1}{\rho_l}\right)\delta_2(\phi) \quad (11)$$

$$\delta_2(\phi) = \begin{cases} 2\delta(\phi), & if\ \phi \leq 0.5\ (gas) \\ 0, & if\ \phi > 0.5\ (metal) \end{cases} \quad (12)$$

$$\rho\left(\frac{\partial \vec{u}}{\partial t} + (\vec{\nabla}\vec{u}).\ \vec{u}\right)$$
$$= \vec{\nabla}.\left[-pI + \mu\left((\vec{\nabla}.\vec{u}) + (\vec{\nabla}.\vec{u})^T\right)\right]$$
$$+ \vec{F}_v + \vec{F}_{inter}.\ \delta(\phi) \quad (13)$$

In the momentum equation (Eq.13), the volume forces $\vec{F}_v$ include gravity, buoyancy, and Darcy's condition (applied only in the metal) while interface forces $\vec{F}_{inter}$ include surface tension as well as Marangoni effect:

$$\vec{F}_v = \rho\vec{g} - \rho\beta(T - T_f)\vec{g} - C\frac{(1 - f_L)^2}{b + f_L^3}\vec{u} \quad (14)$$

$$\vec{F}_{inter} = \sigma\kappa\vec{n} + \vec{\nabla}_S\dot\sigma \quad (15)$$

f_L: liquid fraction

The Darcy condition inhibits fluid flow in the solid phase of the metal. To tend more towards zero velocity, we assigned the solid a dynamic viscosity of 1000 Pa.s.

2.2. Mass-conserving method

At its origin, the LS method was a strictly mathematical approach. One of the drawbacks of two-phase flow simulation with vaporisation is dissatisfaction with the mass-conserving property. A straightforward solution is to add to the right-hand side of the equation (Eq. 11) a fictitious correction quantity of the form:

$$Q_{corr} = \eta_1|m_0 - m(t)|.\ (\phi > 0.5) \quad (16)$$

$m_0[kg]$: initial metal mass; $m(t)[kg]$: metal mass at time t; $\eta_1[1/kg/s]$: a numerical parameter.

This addition is well adapted to this case of welding where experimental mass loss is neglectable and so the metal quantity is very well known.

2.3. Vaporisation modelling

A source term is added to the mass conservation equation to model vaporisation (Eq.11). Esmaeeli and Tryggvason's procedure [7] is repeated, but the Dirac function δ is replaced by δ_2 (Eq.12), which restricts the mass evaporation flux on the gas side and preserves the incompressibility assumption of the liquid metal side.

The intensity of vaporisation is quantified by the retro-diffusion coefficient β_r (Eq.9), which is the flux of particles that recondense by falling back to the interface. β_r depends on the Mach number, which can only be determined by solving the conservation laws across the Knudsen layer. However, β_r is known to take values between 0.18 and 1 [8]. Because of the complexity of the phenomena linked to the Knudsen layer, authors generally assume that $\beta_r = 0.18$ [9], meaning that the intensity of vaporisation is highest with a Mach number $M_a = 1$ in the vapour plume and that the flux of recondensation of the evaporated particles is at the lowest. This remains an ideal case. In practice, deep and unstable keyholes should favour collisions between particles or between particles and the interface so the values of β_r should be higher than the theoretical limit. Based on this reality and without having to face the difficulty of calculating the Mach number, we have assumed an intermediate intensity vaporisation corresponding to $\beta_r = 0.59$ manually calibrated to corroborate experimental observations.

Preliminary calculations have shown that the model underestimated the velocities in the laser-induced plume (<20 m/s) compared to experimental data showing velocities reaching 100-300 m/s next to the liquid-gas interface.

We can explain this mismatch by the fact that a diffuse representation of the liquid-gas interface was chosen. This method does not allow the velocity fields in the molten metal and gas to be calculated separately, even though the two phases have very different properties (factor of 10^3 for volume mass and 10^2 for viscosity), which means that the flow regimes are different. The assumption of laminar flow is, therefore, guaranteed only in the liquid phase.

To better capture the turbulence regime in the plume, Bidare et al. [10] used the RANS SST turbulence model of COMSOL Multiphysics®. Here, we propose an alternative approach consisting of creating turbulence in the vapour plume by using an external force (forcing method [11]) added to the Navier-Stokes equation, and applied only on the gas side:

$$\vec{F}_{forcing} = \eta_2\frac{\dot m}{\rho}\vec{n}.\ (\phi \leq 0.5) \quad (17)$$

η_2 is the forcing coefficient, a numerical parameter enough to get high plume vapour velocity without disturbing the momentum equilibrium at the liquid-gas interface.

This expression of the external force takes into account the mass evaporation flow and makes it possible to simulate very high jet velocities just above the liquid surface where temperatures are higher than the boiling temperature.

2.4. Material properties

Thermophysical properties of aluminium alloy 2219, at solid and liquid phases, are given in Table 1.

3

Table 1. Material properties and numerical parameters

Thermophysical properties of 2219 alloy	Values	Ref.
Thermal conductivity k_{sol}/k_{liq}, [W/m/K]	$k_{sol}(T)/100$	[12]/[13]
Heat capacity $c_{p,sol}/c_{p,liq}$, [J/kg/K]	$c_{p,sol}(T)/1060$	[12]/[14]
Volume mass ρ_{sol}/ρ_{liq} [kg/m^3]	$\rho_{sol}(T)/2400$	[15]/[14]
Dynamic viscosity μ_{liq}[Pa.s]	1.3×10^{-1}	-
Surface tension σ [N/m]	0.96	[13]
Thermocapillary coefficient $\partial\sigma/\partial T$ [N/m/K]	2×10^{-4}	[13]
Solidus, Liquidus, Melting point $T_{sol}/T_{liq}/T_m$ [K]	820/930/875	[14]
Boiling point T_v [K]	2730	[14]
Latent heat of fusion, of vaporisation L_m/L_v [J/kg]	$3.87 \times 10^5/$ 1.08×10^7	[14]
Intrinsic absorptivity A_0	0.25	-
Constants and numerical parameters	Values	Ref.
Retro-diffusion coefficient β_r [-]	0.59	-
Darcy's coefficients C[N.m/(m.m^3)]/ b	$10^7/10^{-3}$	-
Parameter of mass conserving η_1[1/kg/s]	5×10^{10}	-
Parameter of forcing η_2[N.m/(m.m^3)]	2×10^8	-

In the solid-liquid transition domain, thermal conductivity, heat capacity, and volume mass are defined as the average of the solid and liquid properties weighted by the liquid fraction. In the case of heat capacity, the latent heat of fusion is considered to define an equivalent specific heat:

$$c_{p,eq} = c_{p,sol}(1 - HS) + c_{p,liq}HS + \frac{L_m}{\sqrt{\pi \Delta T^2}} exp\left[-\frac{(T - T_m)^2}{\Delta T^2}\right] \quad (18)$$

HS: Heavyside function around the melting point; $2\Delta T = (T_{liq}-T_{sol})$: solidification interval

The gas properties are those of the surrounding air. At the metal-gas interface, equivalent properties are P_{eq} defined as a mixture of metal and gas properties weighted with the LS variable:

$$P_{eq} = P_{gaz} + (P_{metal} - P_{gaz})\phi \quad (19)$$

2.5. Meshing and numerical set-up

The resolution domain is shown in Figure 1. A mapped quadrilateral mesh of 20 μm is applied to a subdomain near the z-axis. The remaining domain is meshed with free triangular elements of around 200 μm.
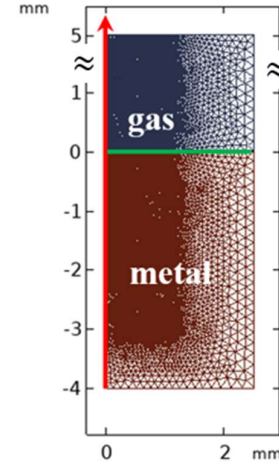

Figure 1. Computational domain and meshing

All governing equations are solved using the direct solver PARDISO in a segregated approach. The implicit temporal scheme BDF is used with a time step of 2 μs. Simulations were run on the 18- core processor Intel® Xeon® W-2295, 3.00 GHz, with 128 GB RAM. The computation time was about 85 minutes per ms of the welding process.

3.   Experimental set-up

The experiments were performed with the disk laser of TRUMPF, Trudisk 6001, λ = 1030 nm. The laser beam analyser FocusMonitor FM+ of PRIMES was used to determine the beam characteristics. The beam radius at the focal plane was calculated according to the 86.5 % law. The calculated value as well as the parameter N_{laser} of the Gaussian law (Eq. 5) were adjusted to better fit with the measured energy distribution. It was found that $r_{laser} = 316 \ \mu m$ at the focus plane and $N_{laser} = 2.15$. The Rayleigh length (Eq. 6) is $z_R = 8.33 \ mm$. Static shots were performed on A2219 alloy plates of 9 mm thickness in the focal

plane ($z = 0$). Every shot was repeated three times with the same operating parameters to investigate the dispersion of the experimental results. The laser beam was slightly inclined to avoid back reflections into the optical cavity. Finally, the temporal pulse shape was monitored. All tests were performed without the supply of shielding gas. The plasma is permanently removed from the laser-matter interaction zone by a jet of compressed air because plasma effects are neglected in the model.

4.   Results and discussion

4.1. Validation of the model

The model is compared to experimental post-mortem results with geometrical criteria.
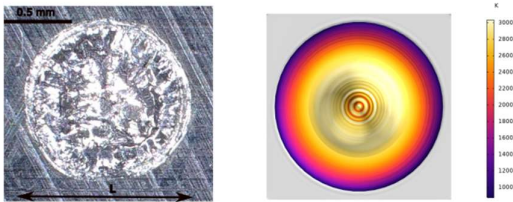
Figure 2. Top view of the melted zone, experimental (left) and numerical (right) with temperature field. $P_{laser} = 4\ kW$, $t = 2\ ms$.
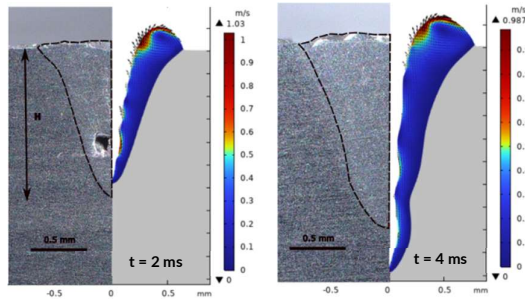

Figure 3. Transversal section of melted zone, experimental (left side) and numerical (right side) with velocity field. The black dashed curve is experimental boundary of the melted zone. $P_{laser} = 4\ kW$, $t = 2\ ms$ and 4 ms.

The diameter of the molten zone (L) was measured on the top surface of the plate after the pulse (Figure 2). A transversal section was then performed at the axis of symmetry of the melted zone to measure it depth (H), Figure 3. The results for $P_{laser} = 4\ kW$ and different pulse times are shown in Figure 4.

The melt pool diameter is well estimated by the model. Regarding depth, good agreement was reached with up to 4 ms. At 6 ms, the depth is overestimated by 30 % compared with the experimental value. However, by observing the
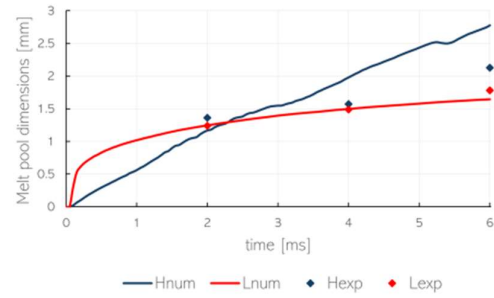

Figure 4. Comparison between experimental and numerical melt pool dimensions. H = depth, L = diameter.

morphology of the melt pool, it appears that the experimental diameter of the melt pool at mid-depth is greater than the same numerical dimension, which implies that the melt pool volumes are close. The cutting technique can also affect the accuracy of the depth measurement, as cutting offset from the axis of symmetry of the melted zone would result in an under-measurement of the experimental depth. Finally, the fact that multiple reflections are not treated means that the laser-matter coupling cannot be accurately modelled. It should also be noted that the model can reproduce the porosities observed in the experiments. Given these experimental data, the model can be considered satisfying and, used to investigate melt instabilities during the laser pulse.

4.2. Formation and dynamics of the melt pool

A thermohydrodynamic analysis of the melt pool means focusing simultaneously on thermal phenomena and liquid metal motion as well as the driving forces involved. The formation and dynamics of the melt pool mainly result from competition between recoil pressure and surface tension forces. We recognise three digging regimes already mentioned in the literature.
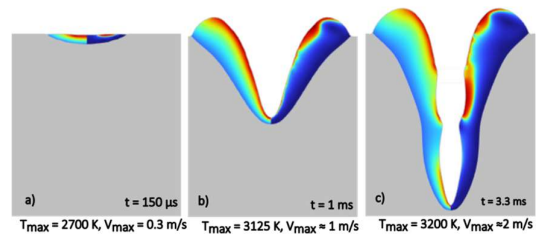

Figure 5. Temperature [K] (left) and velocity [m/s] (right) evolution in the melt pool

Up to 150 μs, the conduction regime where the temperature does not reach boiling point, and the melted zone has a semi-circular shape (Figure 5a). There is no capillary formation, as surface tension forces still predominate. Melt flow is almost negligible.

From 150 μs to 2 ms, the (stable) KH mode is observed with peak temperature at the melt surface

between the boiling point and 3125 K. Recoil pressure becomes predominant, leading to progressive digging of the KH and velocities around 1 m/s (Figure 5b).

Above 2 ms, the force ratio (recoil pressure over surface tension) increases strongly. The capillary takes on a V-shape with some irregularities, a non-smooth melt surface where temperature can reach 3200 K (with some fluctuations), and the velocity 2 m/s (Figure 5c). This regime, which can be termed the "unstable KH mode", will be studied in Sec. 4.3.

4.3. Melt instabilities and resulting porosity

As mentioned above, an unstable melt pool can be characterised by an irregularly shaped capillary, ripples, a strong and violent flow (Figure 5c). Porosity forms during the solidification phase and can have two origins: porosity due to melt instabilities and chemical porosity. We focus here on porosity resulting from melt instabilities.
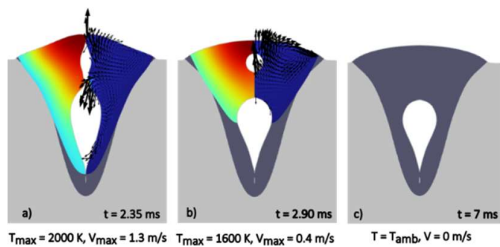

Figure 6. Mechanism of porosity formation. P_{laser} = 4 kW, pulse time = 2 ms. Temperature (left) and velocity (right) fields. The black arrows indicate the direction of the hydrodynamic forces.

We describe the porosity formation mechanism in three steps (Figure 6). Immediately after the pulse, the keyhole collapses, and gas bubbles form. Two bubbles are formed here, a small one at the top and a big one at the bottom. Coalescence of the upper edges of the melt pool occurs at a relatively high velocity (> stable flow velocity during the pulse), indicating a sharp collapse. Resolidification begins at the bottom of the keyhole (Figure 6a). Then comes the stage where the bubble floats. Bubbles behave like bodies immersed in a liquid, subject to two main forces: surface tension and volume forces (gravity and buoyancy). But surface tension predominates. Figure 6b shows that the hydrodynamic forces applied to the small bubble are directed upwards. In contrast, the flows are weak around the large bubble and, moreover, oriented downwards. This is why the small bubble rises and is expelled from the melt pool, whereas the large bubble is almost stationary. Finally, porosity forms when the bubble is definitively trapped, i.e. it does not escape until the surrounding melt has completely resolidified (Figure 6c).

Any method of removing (or reducing) porosity should involve impacting the progression of at least one mechanism stage. How the keyhole collapses is directly related to the nature of the flow regime before laser extinction. For instance, a highly deformed capillary will facilitate the formation of numerous bubbles during the cooling stage. High-energy welding will promote an increase in the molten volume and, as the keyhole collapses at the top while the bubble forms at the bottom, this volume of liquid metal becomes an obstacle to the bubble's ascent. The result is a higher porosity rate in terms of pore number or surface area, as illustrated in Figure 7.
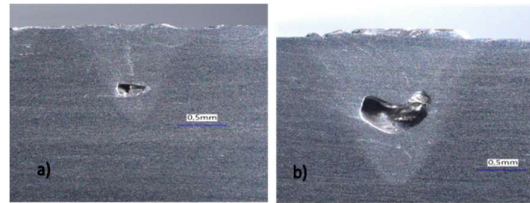

Figure 7. Residual porosities in experiment. P_{laser} = 4 kW, pulse time = 2 ms (a) and 6 ms (b).

Cooling kinetics is also an important factor in the formation of residual porosity since a liquid that solidifies rapidly does not give the gas bubble time to escape. This depends primarily on the material's thermal properties and, that's why the high thermal conductivity of aluminium contributes to porosity defects in laser welding. To produce welds with the desired dimensions and free of porosity defects, it is necessary to work with optimal operating parameters and, in the particular case of aluminium, recent studies suggest that beam shaping is an appropriate method for controlling melt instabilities [16], [17], [18], [19].

5. Conclusions and outlooks

The realistic 2D model developed, including two new ideas concerning the vaporisation simulation and the LS method mass conservation, was used to identify the unstable mode of the melt pool. It was proved that such instabilities contribute to porosity formation. However, modifying the laser parameters can improve the weld quality. Future work should, therefore, focus on the introduction of multiple reflections calculation, for example, to optimise the process through beam shaping. The model must also be upgraded to 3D geometry to accurately address laser-matter coupling during welding with heat source movement.

6. References

[1] A. Matsunawa, J.-D. Kim, N. Seto, M. Mizutani, and S. Katayama, 'Dynamics of keyhole and molten pool in laser welding', *J. Laser Appl.*, vol. 10, no. 6, pp. 247–254, Dec. 1998, doi: 10.2351/1.521858.

[2] M. Courtois, M. Carin, P. Le Masson, S. Gaied, and M. Balabane, 'A complete model of keyhole and melt pool dynamics to analyze instabilities and collapse during laser welding', *J. Laser Appl.*, vol. 26, no. 4, p. 042001, Nov. 2014, doi: 10.2351/1.4886835.

[3] J. Daligault, M. Dal, C. Gorny, F. Coste, and R. Fabbro, 'Combination of Eulerian and ray-tracing approaches for copper laser welding simulation', *J. Laser Appl.*, vol. 34, no. 4, p. 042042, Nov. 2022, doi: 10.2351/7.0000786.

[4] Y. A. Mayi *et al.*, 'An Original Way of Using COMSOL® Application Builder to Enhance Multiphysical Simulation of Laser Welding Processes', 2021.

[5] A. Queva, G. Guillemot, C. Moriconi, C. Metton, and M. Bellet, 'Numerical study of the impact of vaporisation on melt pool dynamics in Laser Powder Bed Fusion - Application to IN718 and Ti–6Al–4V', *Addit. Manuf.*, vol. 35, p. 101249, Oct. 2020, doi: 10.1016/j.addma.2020.101249.

[6] A. Gouffé, 'Corrections d'ouverture des corps noirs artificiels compte tenu des diffusions multiples internes', *Revue d'optique*, 1945.

[7] A. Esmaeeli and G. Tryggvason, 'Computations of film boiling. Part I: numerical method', *Int. J. Heat Mass Transf.*, vol. 47, no. 25, pp. 5451–5461, Dec. 2004, doi: 10.1016/j.ijheatmasstransfer.2004.07.027.

[8] C. J. Knight, 'Theoretical Modeling of Rapid Surface Vaporization with Back Pressure', *AIAA J.*, vol. 17, no. 5, pp. 519–523, May 1979, doi: 10.2514/3.61164.

[9] M. Le Mener, M. Courtois, N. Daviot, M. Carin, and R. Andry, 'Heat transfer and fluid flow modeling of steel-Inconel laser welding in an overlap configuration', *J. Laser Appl.*, vol. 36, no. 4, p. 042006, Nov. 2024, doi: 10.2351/7.0001357.

[10] P. Bidare, I. Bitharas, R. M. Ward, M. M. Attallah, and A. J. Moore, 'Fluid and particle dynamics in laser powder bed fusion', *Acta Mater.*, vol. 142, pp. 107–120, Jan. 2018, doi: 10.1016/j.actamat.2017.09.051.

[11] B. Duret, G. Luret, J. Reveillon, T. Menard, A. Berlemont, and F. X. Demoulin, 'DNS analysis of turbulent mixing in two-phase flows', *Int. J. Multiph. Flow*, vol. 40, pp. 93–105, Apr. 2012, doi: 10.1016/j.ijmultiphaseflow.2011.11.014.

[12] H. X. Wang, Y. H. Wei, and C. L. Yang, 'Numerical simulation of variable polarity vertical-up plasma arc welding process', *Comput. Mater. Sci.*, vol. 38, no. 4, pp. 571–587, Feb. 2007, doi: 10.1016/j.commatsci.2006.03.017.

[13] Y. Zhang, Z. Shen, and X. Ni, 'Modeling and simulation on long pulse laser drilling processing', *Int. J. Heat Mass Transf.*, vol. 73, pp. 429–437, Jun. 2014, doi: 10.1016/j.ijheatmasstransfer.2014.02.037.

[14] C. Liu and J. He, 'Numerical analysis of fluid transport phenomena and spiking defect formation during vacuum electron beam welding of 2219 aluminium alloy plate', *Vacuum*, vol. 132, pp. 70–81, Oct. 2016, doi: 10.1016/j.vacuum.2016.07.033.

[15] K. Narender, A. S. M. Rao, K. G. K. Rao, and N. G. Krishna, 'Thermo physical properties of wrought aluminum alloys 6061, 2219 and 2014 by gamma ray attenuation method', *Thermochim. Acta*, vol. 569, pp. 90–96, Oct. 2013, doi: 10.1016/j.tca.2013.07.003.

[16] K. Mathivanan and P. Plapper, 'Laser welding of dissimilar copper and aluminum sheets by shaping the laser pulses', *Procedia Manuf.*, vol. 36, pp. 154–162, 2019, doi: 10.1016/j.promfg.2019.08.021.

[17] S. Geng, W. Yang, P. Jiang, C. Han, and L. Ren, 'Numerical study of keyhole dynamics and porosity formation during high-power oscillating laser welding of medium-thick aluminum alloy plates', *Int. J. Heat Mass Transf.*, vol. 194, p. 123084, Sep. 2022, doi: 10.1016/j.ijheatmasstransfer.2022.123084.

[18] A. Sadeghian and N. Iqbal, 'A review on dissimilar laser welding of steel-copper, steel-aluminum, aluminum-copper, and steel-nickel for electric vehicle battery manufacturing', *Opt. Laser Technol.*, vol. 146, p. 107595, Feb. 2022, doi: 10.1016/j.optlastec.2021.107595.

[19] Y. Ai, J. Liu, C. Ye, and J. Cheng, 'Influence of oscillation parameters on energy distributions and dynamic behaviors during laser welding of aluminum alloy T-joints assisted with solder patch', *Int. J. Therm. Sci.*, vol. 201, p. 108953, Jul. 2024, doi: 10.1016/j.ijthermalsci.2024.108953.